BNL-221097-2021-JAAM

Self-re-adhering alkali-activated cement composite and its ability to mitigate corrosion of carbon steel in 300oC hydrothermal environment

T. Sugama

To be published in "Geothermix"

February 2021

Interdisciplinary Science Department

Brookhaven National Laboratory

U.S. Department of Energy

USDOE Office of Energy Efficiency and Renewable Energy (EERE), Geothermal Technologies Office (EE-4G)

DISCLAIMER

Article

Self-re-adhering alkali-activated cement composite and its ability to mitigate corrosion of carbon steel in 300°C hydrothermal environment

Toshifumi Sugama [1], Tatiana Pyatina [2,*]

[1] Brookhaven National Laboratory; sugama@bnl.gov
[2] Brookhaven National Laboratory; tpyatina@bnl.gov
* Correspondence: tpyatina@bnl.gov; Tel.: +1-631-681-3725

Received: date; Accepted: date; Published: date

Abstract: Cement- steel interface is a weak point of cement sheath integrity under the environments of high-temperature geothermal wells. This paper presents carbon steel (CS) adherence behaviors of 300°C-autoclaved alkali-activated Calcium-Aluminate-Cement (CAC)/fly ash F (FAF) (Thermal Shock Resistant Cement, TSRC), granulated blast furnace slag (GBFS)/SiO_2, and Ordinary Portland Cement (OPC)/SiO_2 blends. The composites' ability to preserve the bond under the conditions of thermal shock (TS) and strong acid attack (pH 0.6 H_2SO_4/brine at 90°C) as well as their ability to recover the damaged bond and provide steel corrosion protection after additional short-time 5-day curing at 300°C were evaluated. GBFS/SiO_2 sheath underwent catastrophic failure in the first TS cycle; OPC/SiO_2 lost 78% and TSRC 51% of the bond strength in 6 cycles. Only TSRC-CS bond survived 30 days of strong acid exposure; OPC/SiO_2 bond failed after 18 days and GBFS/SiO_2 after 20 days. Addition of micro-glass fibers (MGF) to TSRC further improved its bond strength and CS corrosion protection. Samples of TSRC-CS cured for 30 days at 300°C before the bond damage recovered 49% of the damaged bond strength after additional short-time curing. The CS protected by the re-adhered TSRC showed low corrosion rate of 0.13 mm/year (TSRC-MGF), 0.2 mm/year (TSRC) vs. 0.64 mm/year for OPC/SiO_2 protected CS.

Keywords: alkali-activated cement; cement-carbon steel bond; acid resistance; thermal shock resistance; slag

Abbreviations:

ASR – alkali silica reactions
ATR-FTIR - Attenuated Total Reflectance-Fourier Transform Infrared Spectroscopy
CAC - calcium-aluminate cement
CS – carbon steel
FGP – fine glass powder
EDX - energy dispersive x-ray
FAC/FAF- fly ash type C or F
GBFS - granulated blast furnace slag
MCF/MGF - micro- carbon or glass fibers
OPC - Ordinary Portland Cement
SMS - sodium meta-silicate
TSRC - Thermal Shock Resistant Cement
XRD - x-ray powder diffraction
YM - Young's modulus

1. Introduction

This is the second paper on self-healing of high-temperature geothermal cements. The first paper addressed self-healing behavior of cement matrix (Pyatina and Sugama 2020). This one looks at the cement-carbon steel (CS) interface durability and cement self-re-adhering ability to CS after the bond damage under conditions of high-temperature geothermal wells. Although geothermal wells are difficult for cements to survive in general due to the chemical, mechanical and thermal stresses, the bond between cement and metal casing is particularly vulnerable to degradation in such wells. Even for cements possessing good bond durability, the extreme thermal and mechanical stresses in cement/casing interfacial boundary regions can cause debonding of cement from casing surfaces(Kaldal et al. 2015, 2016; Lecampion et al. 2011; Wise et al. 2020). Such interfacial bond failure not only engenders a lack of well casing integrity, but also promotes corrosion of the casing (Amin et al. 2009; Teodoriu et al. 2013; Zhijun, Yanjun, and Jianghong 2013). An ideal solution for this issue would be self-re-adhering of debonded cement to CS casing.

Low-temperature studies of various alkali-activated blends that included fly ash showed improved metal bonding due to the increase in the formation of dense amorphous calcium-silicate hydrate and, depending on the nature of the blend and the activator, some sodium-aluminum-silicate hydrate at the interface (Phoo-ngernkham et al. 2020; Phoo-Ngernkham et al. 2015, 2017; Wolfe 2011). To the best of our knowledge the re-adherence of high-temperature blends that involve calcium-aluminate cement has not been reported.

Previous studies have demonstrated good cement matrix self-healing ability of alkali activated calcium-aluminate cement/Fly Ash F blend (Thermal Shock Resistant Cement, TSRC) under high temperature geothermal conditions (300^{o}C, water, alkali carbonate, geothermal brine)(Pyatina and Sugama 2019, 2020; Tatiana Pyatina, Sugama, and Ronne 2016). The blend was able to recover more than 85% of strength both after a short 1 day- and a longer 30-day curing period demonstrating good acid and thermal shock resistance when compared with Ordinary Portland Cement (OPC) high-temperature blend with silica, alkali-activated granulated blast furnace slag blend with silica, alkali-activated blend of fly ash F and C(Pyatina and Sugama 2020). The self-healing performance of all tested composites was further improved with micro glass fibers and the crack size and propagation were controlled with micro-carbon fibers (MCF).

Although TSRC matrix was shown to be readily self-healing under geothermal conditions, the other indispensable factor governing geothermal well integrity is the requirement of an adequate bond durability at interfaces between the cement and metal casing. A previous work on a cement/metal joint system demonstrated that two factors played a pivotal role in improving the adhesive force of 300°C-autoclaved MCF-modified TSRC composites to CS casing and creating a tough interfacial bond structure at the composites/CS interface under the 7-cycle 350°C heat→ 25°C water cooling-induced tensional stresses (Pyatina, Sugama, and Zaliznyak 2017; Sugama and Pyatina 2017). The first factor was the formation of Fe-containing interfacial reaction products in the critical boundary regions between TSRC and CS; in particular, the crystalline brownmillerite [$Ca_2(Al, Fe^{+3})_2O_5$] phase in TSRC. The amount of brownmillerite reaction product between composites and CS increased with the extension of the number of heat-cooling thermal tensional stress cycles, thereby resulting in the enhanced coverage of CS surfaces by the composites adhering to CS after a shear bond testing. This fact strongly suggested that the adhesive force of composites to CS was greater than the strength of the composite itself. The other factor was the strong effect of MCF on enhancing the shear bond tensile extension more than two-fold, compared with that of the cements without MCF, highlighting that MCF played a pivotal role in significantly improving the bond durability between composite and CS. By contrast, the hydration products of the 300°C-autoclaved OPC, Class G/SiO_2, had no significant effect on improving the shear bond strength and the bond's toughness. These crystalline products mostly consisted of xonotlite, 0.9 nm-tobermorite and –riversideite. No chemical interaction products with CS were found in the cement adhered to CS after the shear bond testing.

In the present work, we continued evaluation of the three MCF-reinforced alkali-activated cement composites with and without E-type micro glass fiber (MGF) as self-re-adhering aid. One was

TSRC and the other two were pozzolan-based alkali-activated cements, Class C (fly ash C, FAC)/FAF and GBFS/SiO_2 blends, possessing the hydrothermal- and thermal stability of ≥300°C. For comparison, we adapted the conventional calcium silicate OPC, Class G well cement modified with SiO_2, MCF and MGF as reference composite samples. The objectives of this project were: 1) to evaluate bond durability of these composites under thermal shock and acidic brine environments, 2) to measure interfacial bond strength and identify bond failure modes at composite /CS interface, 3) to investigate whether composites adhering to CS surfaces at early hydration age at 300°C adequately protect the CS from corrosion, 4) to select the most effective alkali-activated composite in bond durability and adhesion from among different composite systems for the self-re-adhering performance of debonded composite to CS surfaces, 5) to obtain fundamental understanding of self-re-adhering mechanisms and key factors affecting bond durability, and 6) to assess the ability of the re-adhered composites to protect CS against brine-caused corrosion.

2. Materials and Methods

2.1. Starting Materials

The detailed information on the starting materials can be found elsewhere (Pyatina and Sugama 2020). The two cement binders, CAC, Secar #80 and OPC, Class G were supplied by Kerneos Inc. and Schlumberger, respectively. The X-ray powder diffraction (XRD) data showed that the crystalline compounds of #80 CAC included the following three principal phases, calcium monoaluminate ($CaO.Al_2O_3$, CA), calcium dialuminate ($CaO.2Al_2O_3$, CA_2) and corundum (α-Al_2O_3), while OPC consisted of hatrurite ($3CaO.SiO_2$) as major, and brownmillerite ($4CaO.Al_2O_3.Fe_2O_3$), basanite ($CaSO_4.1/2H_2O$) and periclase (MgO) as minor phases. The sodium metasilicate (SMS, Na_2SiO_3) powder of 93% purity with the particles' size of 0.23- to 0.85-mm was supplied by the PQ Corporation under the trade name of "Metso Beads 2048" and was used as an alkali activator. It had a 50.5/46.6 Na_2O/SiO_2 weight ratio. To improve the compressive toughness, and suppress and control the post-stress crack opening and crack width, micro carbon fiber (MCF) under the trade name of AGM-94 derived from a polyacrylonitrile (PAN) precursor, supplied by Asbury Graphite Mills, Inc was added to all cement formulations. It was 7-9 μm in diameter and 100-200 μm in length, and its visual appearance was a powder-like product. Five different pozzolans were used: silica flour as a natural pozzolan, Class F (FAF) and C (FAC) fly ashes, granulated blast furnace slag (GBFS) as an industrial by-product, and E-type MGF as an artificial pozzolan. The silica flour was supplied by U.S. Silica Company. Of the three industrial by-products, FAF, FAC, and GBFS, the first two products were provided by Boral Material Technologies, and the GBFS was manufactured by Lafarge North America Inc. The XRD analysis for these by-products revealed that the FAF included three major crystalline phases, quartz (SiO_2), mullite ($3Al_2O_3.2SiO_2$), and hematite (Fe_2O_3), the three major phases of the FAC were tricalcium aluminate ($3CaO.Al_2O_3$, C_3A), quartz, and calcium sulfate anhydrate ($CaSO_4$); the GBFS was essentially amorphous. The artificial pozzolanic product, powdery MGF under the trade name of "Microglass 7280" as calcium aluminosilicate E-type MGF, was supplied by Fibertec and it had a diameter of 16 μm and a length of 120 μm.

2.2. Formulas of cement composites

All composites were prepared as dry blends with MCF as a reinforcement at 6wt/%. The OPC/SiO_2 blend consisted of 70wt% OPC, Class G and 30wt% silica flour (SiO_2). In the TSRC, the #80/FAF ratio was 60/40 by weight; both the SMS alkali activator and the MCF were incorporated at 6% by the total weight of the #80/FAF dry blend. The same amount of SMS and MCF also was used for two other alkali-activated composites: 60wt% FAC/40wt% FAF and 70wt% GBFS/30wt% SiO_2 blends. The amount of SMS was chosen to provide the highest compressive strength for the tested cement systems after an autoclaving for 24hrs at 300°C. Some of the samples were dry blended with 3% MGF by total mass of the blend as a self-re-adhering aid. In all MGF-modified composites, MCF content was reduced to 3% from 6%. The water/cement (W/C) ratios to make similarly self-leveling composite slurries were as follows: 0.48 for OPC/SiO_2; 0.51 for TSRC; 0.46 for FAC/FAF; and, 0.45 for

GBFS/SiO_2. It should be noted that the W/C ratio of slurries with 6wt% MCF without MGF was the same as in the slurries with 3wt% MCF/3wt% MGF.

2.3. Samples preparation

To observe crack formation and propagation in composite sheath, caused by its debonding from CS casing surfaces, unconfined composite sheath samples surrounding CS tubes were prepared in the following sequence. The disk-shaped wooden tube-holder (48-mm-diam. by 13-mm-high) with a center hole (26- mm-diam.) was placed at the bottom of the cylindrical paper-mold with 49-mm-inner diameter and 100-mm length. A CS tube (125-mm-long x 25-mm-outer diam. x 3-mm-wall thickness) was inserted into the center hole of the wooden casing holder located at the bottom of the mold. The hand-mixed composite slurry was poured in an annular space between the tube and the mold to prepare a sheath sample of 23 mm thick and 74 mm high. Next, the samples were pre-cured for 24 hours under 99±1% relative humidity at 85°C to imitate the temperature regime of cement placement into a well. The pre-cured sheath sample was removed from paper mold and autoclaved for 24 hours at 300°C under the pressure of 8.3 MPa. The autoclaved sheath samples were used for measuring the sheath shear-bond strength. The lap-shear adhesion test was conducted to determine the adhesive force of the composite coupling between CS plates according to modified ASTM D5868. The AISI 1008 cold rolled steel test panel was used for this test. It was supplied by ACT Test Panels, LLC. Prior to cement bonding tests, CS plates were immersed in 5 wt% alkali-cleaning solution (Alkaline cleaner #4429, supplied by American Chemical Products) at 40°C for 10 min to remove surface contaminants, and then, the surfaces of the alkali-cleaned panels were rinsed with tap water at 25°C, followed by drying for 24 hours in the air. In preparing these samples, two plates, 32-mm-wide by 100-mm-long and 0.9-mm-thick each, were bonded together with a layer of cementitious composite; the overlapped area connected by the cement layer was 1440 mm^2 (45-mm-long by 32-mm-wide). The joint was pre-cured for 24 hours at 85°C, 99±1% relative humidity under a loading of 16 g, and then it was autoclaved without any loading at 300°C for 24 hours before the lap-shear bond test. To assess the acid-resistance of the composites, the 300°C-autclaved samples were immersed in a pH 0.6 H_2SO_4-modified geothermal brine at 90°C. The lap-shear bond plates of carbon steel with the thin cement layer in between were covered with epoxy resin (Epoxy Systems, Inc., product #633) to protect the exposed parts of carbon steel from the acid attack. The edges of the samples remained uncovered, so the narrow strips of cement were exposed to the acid. Such a low starting pH was chosen to accelerate the cement damage since only a small part of the cement (edges of the samples) was in direct contact with the acid. Composition of the brine can be found elsewhere (Sugama and Pyatina 2019b). The total dissolved solids concentration in brine was 242490 mg/L with chlorine concentration being 13.5%.

2.4. Measurements

Electromechanical Instron System Model 5967 was used to obtain mechanical properties including sheath-shear bond strength, and lap-shear bond strength. XRD (40 kV, 40 mA copper anode X-ray tube), Attenuated Total Reflectance-Fourier Transform Infrared Spectroscopy (ATR-FTIR), Energy Dispersive Micro X-ray Fluorescence Spectrometer (μEDX), and Raman confocal microspectrometer equipped with Leica® DM2700™ upright microscope in non-destructive Raman chemical state mapping experiments were used to identify amorphous and crystalline phase compositions and transitions responsible for improving bond durability. The results of XRD tests were analyzed using PDF-4/Minerals 2015 database of International Center for Diffraction Data (ICDD).

The extent of the self-re-adherence of 300°C-autoclaved CS-composite-sheath samples was determined by measuring the recovery of sheath-shear bond strength after the additional 5-day-300°C-autoclaving of debonded sheath samples. We also attempted to measure the recovery of lap-shear bond strength at CS plate /composite adhesive/CS plate joint. In this attempt, the two debonded CS plates were physically reattached by a steel wire, and autoclaved for 5 days at 300°C. After the

194 autoclaving, the steel wire was removed from samples to assess whether the plates re-bonded.
195 However, unlike for the sheath samples(Pyatina and Sugama 2020), the shear strength of the re-
196 attached lap samples was too weak to be measured. Therefore, the samples were used to identify the
197 locus of bond failure in the critical interfacial boundary regions between CS and the composite, and
198 to estimate the thickness of composite adhesive before and after the re-adherence treatment using
199 Absolute Digimatic Caliper by Mitutoyo Corp. For the latter, the thickness was measured in seven
200 different locations on each debonded CS plate.
201 After the lap-shear bond tests the plate with the thinner cement layer was used to determine the
202 corrosion rate of CS. The thickness of composite layers over CS correlated directly with the corrosion
203 rate of the underlying CS. To obtain information on the protection of CS by composite against brine-
204 caused corrosion, DC electrochemical testing for the underlying CS was performed using the
205 Princeton Applied Research Model Versa STAT 4 Corrosion Measurement System. In this
206 assessment, the CS plates used in the lap-shear bond tests, with composite-adhered and re-adhered
207 to its surface, were mounted into a holder, and then inserted into the Ametex Model K0235 flat cell
208 containing a 1.0 M sodium chloride electrolyte solution. The test was conducted under an aerated
209 condition at 25°C, on an exposed surface area of 1.0 cm^2. The polarization curves were measured at a
210 scan rate of 0.17 mVs^{-1} in the corrosion potential range from -0.4 to +0.6 V. The average corrosion rate,
211 mm/year (mmpy), associated with the corrosion potential, $E_{corr.}$, mV, and corrosion current density,
212 $I_{corr.}$, μA, was obtained by averaging Tafel fit results of the polarization curves of three samples.

213 **3. Results**

214 *3.1. Lap-shear bond strength, bond failure mode, and corrosion mitigation tested on composite/CS plate joints*

215
216 Figure 1 presents the lap-shear bond strength of four different MGF-free composites. The
217 samples were tested after 1-day autoclaving at 300°C. As seen in the figure, alkali-activated composite
218 adhesives had a far greater bonding strength than the OPC-based composites. The shear bond
219 strength decreased in the following order: GBFS/SiO_2 (1.64MPa) > TSRC (1.41MPa) > FAC/FAF
220 (1.23MPa)> OPC/SiO_2 (0.4MPa). The bond strengths of the first two composites, GBFS/SiO_2 and TSRC,
221 were more than 3.5-times higher than that of OPC/SiO_2.

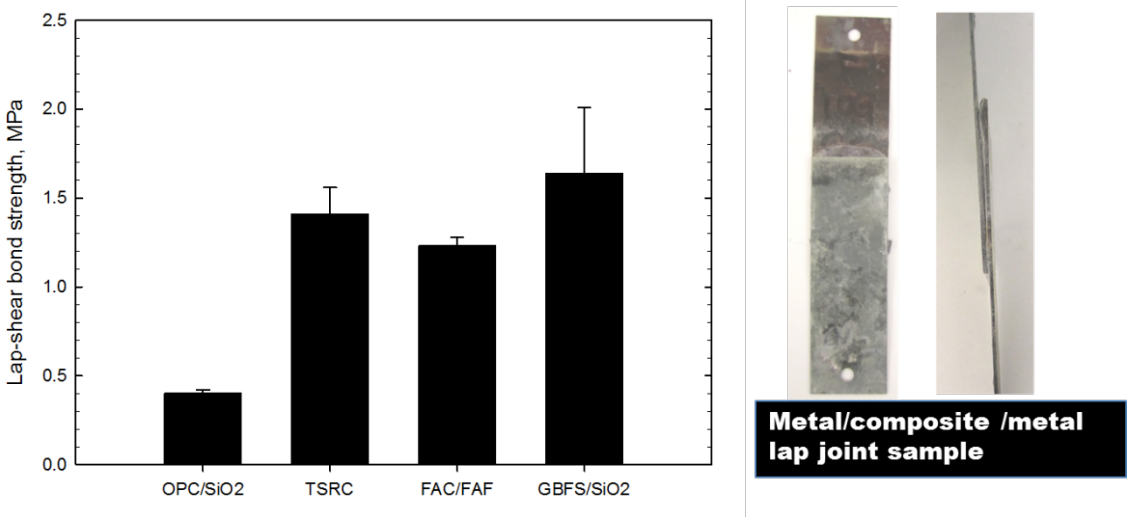

222
223 **Figure 1.** Lap-shear bond strength of MGF-free composites made by 1-day autoclaving at 300°C.

224 There are three different bond failure modes: 1) a cohesive failure that takes place in a composite
225 layer, 2) an adhesive failure that happens at the interfaces between a composite and CS, and 3) the 1)
226 and 2) mixed failure (Sugama and Pyatina 2019a). The most ideal failure is the cohesive one, which
227 happens when the bond strength of the composite to CS is higher than the strength of the composite

itself, so the bond breaks in the composite. In this mode even after the bond failure the CS is still protected from corrosion with some layer of the composite. As is evident, the OPC-based composites (Figure 2) disclosed a poor bonding behavior with the failure for the most part occurring at the interface and only partially in the composite. The presence of these adhesively failed areas was the major reason for the weak shear-bond strength (0.4 MPa) of the OPC-based composites. FAC/FAF showed the mixed failure mode. Corrosion stains were visible on the CS protected by these two composites already after a day of high-temperature autoclaving confirming their inadequate bonding behavior (Figure 2). The corrosion was caused by the following three factors: 1) a poor bond behavior, 2) undesirable chemistry of the composites and 3) porous microstructure of the composite layers adhering to CS.

OPC- and fly ash-based composites did not provide a sufficient protection of CS against corrosion. In contrast, alkali-activated TSRC and GBFS/SiO_2 composites along with a great bond strength revealed the ideal composite coverage over the CS surfaces; namely, the surfaces of both CS sites were completely covered with these composites after the bond failure. Thus, the interfacial bond failure occurred in a composite layer as a cohesive bond failure mode (Figure 2). There were no significant corrosion spots on the CS covered by these composites. Both TSRC and GBFS/SiO_2 effectively mitigated corrosion of the CS.

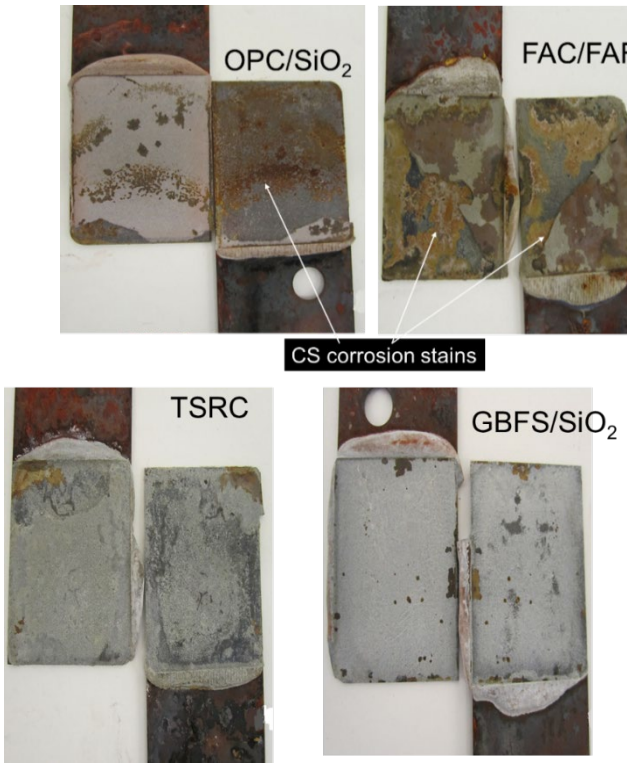

Figure 2. Appearance of the debonded OPC/SiO_2, FAC/FAF, TSRC, and GBFS/SiO_2 composites covering CS plates.

3.2. Bond durability of composites adhered to CS under cyclic thermal shock stresses

Composite sheath samples autoclaved at 300°C for 1 day were tested in 6-cycle thermal shock stress tests (one cycle: 350°C heating for 24 hours, and then cooling by passing 20°C water through the inner CS casing for 10 minutes). Three composites (TSRC, GBFS/SiO_2, and OPC/SiO_2) were evaluated. Figure 3 depicts the unconfined sheath-shear bond strength for these composites before

and after the thermal shock tests as well as the loss of the bond strength after the thermal shock. The GBFS/SiO_2 sheath generated cracks after 300°C-1-day autoclaving, possibly due to the sample shrinkage. The sheath-shear bond strength of this composite was only 0.26 MPa. Furthermore, the catastrophic bond failure was observed in the first thermal cycle test of the GBFS/SiO_2 samples.

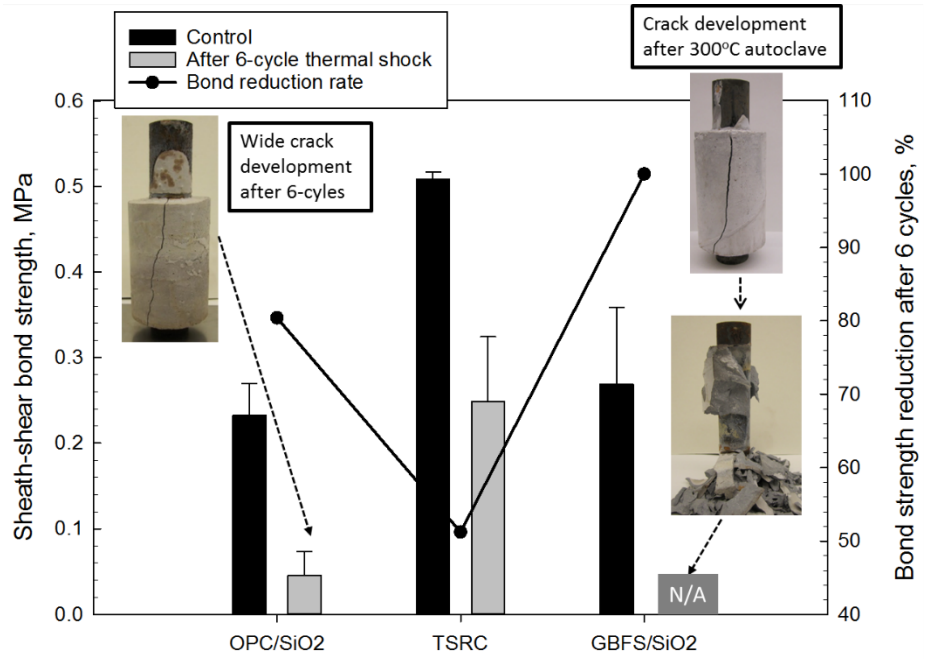

Figure 3. Unconfined sheath-shear bond strength for composites before and after 6 cycles of thermal shock.

The two other composites did not develop cracks after the autoclaving. The thermal shock reduced the original TSRC sheath-shear bond strength of 0.51 MPa by 51% to 0.25 MPa. By contrast, the OPC/SiO_2 reference composite strikingly lost the bond strength, which decreased from 0.23 MPa before the shock to 0.05 MPa after the shock, corresponding to nearly 80% reduction. After the 6 cycles, this composite developed wide cracks. Thermally shocked samples of TSRC possessed the bond strength of more than 5 times higher than that of the OPC/SiO_2 reference composite, strongly demonstrating great bond durability of TSRC with CS under the thermal shock environment.

3.3. Bond durability of composites adhered to CS under pH 0.6 H_2SO_4/brine environment at 90°C

The bonds of different composites collapsed after different exposure times. All composites lost some strength under such hot acidic brine conditions in the first 15 days (Figure 4). Extended exposure of 30 days caused a dramatic decrease in the bond strength for two composites, OPC/SiO_2 and GBFS/SiO_2. As seen in the photographs, OPC/SiO_2 adhesive layers for the most part eroded after an exposure of 18 days, engendering a catastrophic interfacial bond failure. The bond failure mode of GBFS/SiO_2 differed from that of OPC/SiO_2; the acidic brine erosion was minor for GBFS/SiO_2. Instead, the interfacial boundary region underwent an adhesive degradation through interactions with the acid and salts precipitation in the boundary region after the 20-day exposure, thereby resulting in the interfacial debonding of the composite from CS.

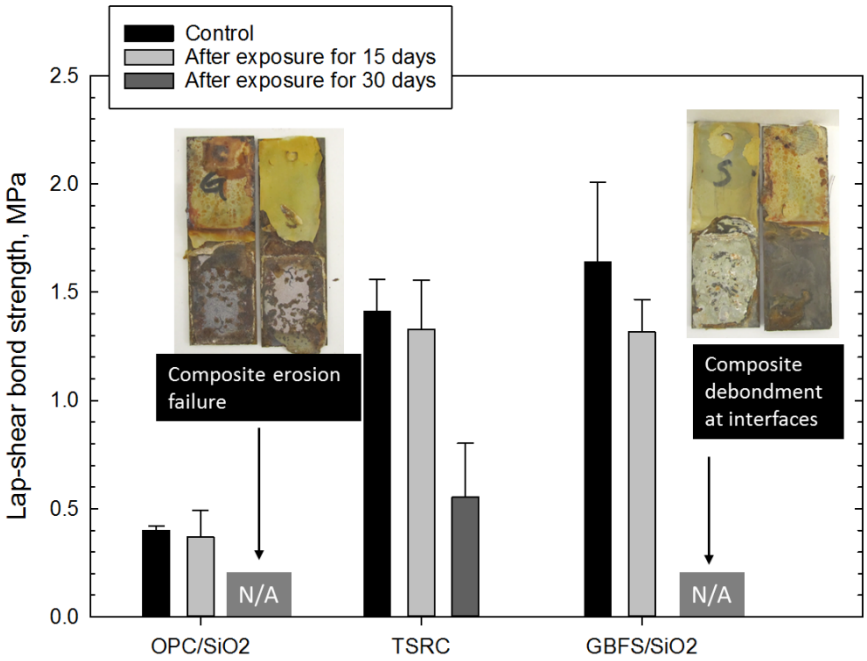

Figure 4. Bond durability in pH 0.6 H_2SO_4/brine environment at 90°C for up to 30-day exposure.

In contrast, TSRC adhesive remained in effect for the 30-day exposure, and with the remaining lap-shear bond of 0.55 MPa, strongly underscoring a great resistance to a pH 0.6 acid/brine at 90°C of the bond structure at the interfaces between TSRC and CS and an outstanding bond durability in such a harsh environment.

To obtain a better understanding of cement degradation in acidic brine for these three adhesives, some additional studies were done using the combined analytical tools of XRD, μEDX, FT-IR, and Raman imaging.

3.3.1. Crystalline phase identification – XRD

Table 1 shows identified crystalline phases along with their ICDD numbers for the samples which were collected by scrubbing the adhesives covering from the CS plate surfaces after acid-exposure tests. The OPC/SiO_2 and GBFS/SiO_2 samples were taken after 18- and 20-day acid exposure, respectively, after the bond failure, while the TSRC sample was collected after 30 days of the exposure. All specimens contained some magnetite from the CS (not included into the table). The change in the crystalline composition of the samples could be attributed to the formation of new phases as a result of the acidic brine exposure and as a result of continuous curing at 90°C(Alexander 1960). The acid exposure leads to the presence of sulfonated products (both amorphous and crystalline), while the continuous curing makes the phases stable at that temperature.

Table 1. Crystalline phase compositions of the cement composite samples between two CS plates, exposed to 90°C- pH 0.6 sulfuric acid/brine for TSRC, OPC/SiO_2 and GBFS/SiO_2 composite adhesives.

Principal phases	Secondary phases
TSRC control	
Corundum Al_2O_3 (04-002-3621)	Hedenbergite $CaFeSi_2O_6$ (04-013-2079)
Mullite $Al_{2.26}Si_{0.74}O_{4.87}$ (04-016-1587)	Calcite $CaCO_3$ (00-005-0586)
Grossite $CaAl_4O_7$ (00-023-1037)	Sodalite $Na_6Al_6(SiO_4)_6$ (04-009-5260)
Cristobalite-II/quartz SiO_2 (04-018-0238/01-070-7345)	Analcime $Na(AlSi_2O_6)H_2O$ (01-074-2218)
	BoehmiteAlOOH (01-074-2898)

Garronite $Na_{0.8}Ca_{2.82}(Al_6Si_{10}O_{32})(H_2O)_{12.08}$ (01-079-1336) Dmisteinbergite $Ca(Al_2Si_2)O_8$ (00-051-0064)	
TSRC after the acid exposure for 30 days	
Corundum Al_2O_3 (00-005-0712) Garronite $Na_{0.8}Ca_{2.82}(Al_6Si_{10}O_{32})(H_2O)_{12.08}$(01-079-1336) Dmisteinbergite/anorthite $Ca(Al_2Si_2)O_8$ (00-031-0248/00-041-1486) Silicon oxide SiO_2 (01-073-2991) Analcime $Na(AlSi_2O_6)H_2O$ (01-074-2218)	Anhydrate $CaSO_4$ (04-007-4744) Hedenbergite $CaFeSi_2O_6$ (04-013-2079) BoehmiteAlOOH (01-74-2898) Sodalite $Na_6Al_6(SiO_4)_6$ (04-009-5260)
OPC/SiO_2 control	
Xonotlite $Ca_6Si_6O_{17}(OH)_2$ (00-023-0125/01-074-7586) Tobermorite 9A $Ca_5Si_6O_{17}(OH)_2$ (04-012-1761)	Quartz SiO_2 (01-075-8320)
OPC/SiO_2 after the acid exposure for 18 days	
Xonotlite $Ca_6Si_6O_{17}(OH)_2$ (00-023-0125); Riversideite-9A (00-029-0329)	Coesite/Quartz SiO_2 (04-015-7165/00-033-1161)
GBFS/SiO_2 control	
Xonotlite $Ca_6Si_6O_{17}(OH)_2$ (00-023-0125); Quartz SiO_2 (04-008-7653); Tobermorite 11A (00-019-1364); Diopside, sodian, aluminian $Na_{0.3}Ca_{0.65}Mg_{0.65}Fe_{0.1}Al_{0.3}Si_2O_6$ (04-013-2121)	Calcite $CaCO_3$ (04-007-0049)
GBFS/SiO_2 after the acid exposure for 20 days	
Silica/coesite SiO_2 (01-075-8322/01-072-1601); Xonotlite $Ca_6Si_6O_{17}(OH)_2$ (00-023-0125); Bassanite $CaSO_4$ 0.67 H_2O (00-047-0964)	Diopside ferroan (01-087-2070); $(Mg_{0.39}Fe_{0.52}Ca_{0.09})SiO_3$ (01-071-0712); Tobermorite 11A $Ca_5Si_6O_{17}(OH)_2$ (00-019-1364); Millosevichite $Al_2(SO_4)_3$ (04-005-9668) Calcite $CaCO_3$ (01-072-1937)

For the TSRC, non-reacted crystalline mullite was still present in the control sample, cured for a day at 300°C (Figure 5). The peaks of dmisteinbergite, boehmite and analcime were small while grossite was the major calcium-aluminate hydrate. After the continuous curing during the 30-day exposure to the acid dmisteinbergite and analcime became the major crystalline phases as was expected based on the previous studies (Misaelides P, Godelistas A Link F 1991, 2016). The changes related to the interactions with the acid included a decrease in the content of such calcium-containing phases as garronite (significant decrease of the major peak intensity at 2θ° 28.28) and calcium carbonate (complete disappearance of the peak at 2θ° 29.38). Identification of the cement-acid reaction products was problematic due to the complexity of the XRD patterns. The fitting program SIeve+ of the International Center for Diffraction data suggested a possibility of calcium, aluminum and iron sulfates in the sample (Anhydrate $CaSO_4$ (04-0070-4744), Millosevichite $Al_2(SO_4)_3$ (04-005-9668), Szomolnokite $FeSO_4(H_2O)$ (00-021-0925). However, their patterns strongly overlap with the pattern of analcime that clearly increased in intensity after the 30-day exposure. The presence of anhydrate in the exposed sample is likely since there was a noticeable rise in the intensity of the shoulder at 2θ° 31.36 in comparison with the control pattern. The presence of iron sulfate could be argued based on the peak at 2θ° 35.56. As for aluminum sulfate it could not be identified unambiguously in these experimental patterns. Additionally, the baseline of the acid-exposed sample increased suggesting higher content of amorphous phases and a decreased sample's crystallinity.

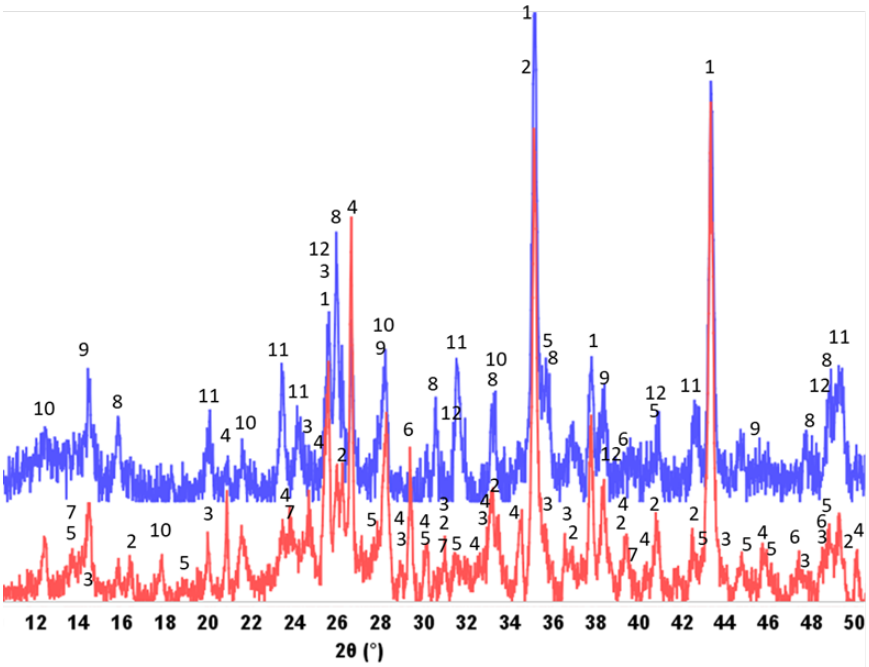

Figure 5. XRD patterns of TSRC before (bottom) and after (top) the 30-day acid exposure. 1-corundum, 2-mullite, 3-grossite, 4 quartz, 5-hednbergite, 6-calcite, 7-sodalite, 8-analcime, 9-boehmite, 10-garronite, 11-dmisteinbergite, 12-anhydrate.

The major change in the pattern of the OPC/SiO_2 cement exposed to the acid environment was a significant reduction in intensity of the quartz peak at 26.72° (Figure 6). This could be a result of continuous cement hydration with formation of calcium-silicate hydrates. After the acid exposure there was a slight decline in intensities of xonotlite, the major calcium-silicate hydrate. Formation of calcium sulfate could not be confirmed decidedly; although bassanite presence at low concentrations was proposed by the SIeve+ fitting program. Despite little changes in the crystalline composition, the bond of this cement broke in the first 18 days under the acidic conditions, partially because of the low initial bond strength.

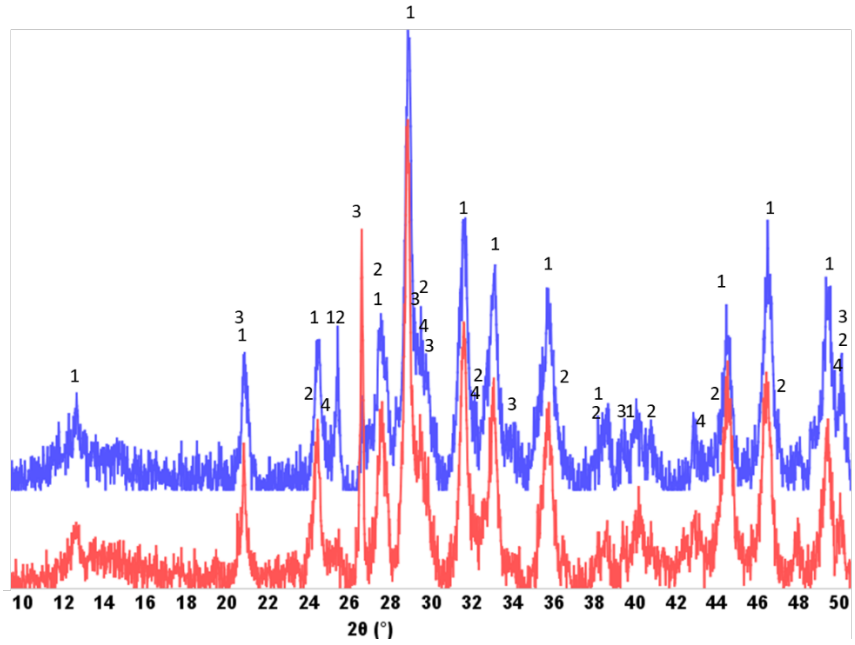

Figure 6. XRD patterns of OPC/SiO_2 blend before (bottom) and after (top) the 30-day acid exposure. 1-xonotlite, 2-tobermorite, 3-quartz, 4-riversideite-9A.

The GBFS/SiO_2 samples clearly showed bassanite in their composition (new peaks at 2θ°: 14.69, 29.71, 31.97) after the acid exposure (Figure 7). A new small peak around 2θ° 25.53 could be attributed to aluminum sulfate (04-005-9668). Formation of bassanite corresponded to the decrease in intensities of calcium-silica hydrates (xonotlite and tobermorite) that decomposed by loss of calcium. The intensity of calcite peaks also decreased (major peak at 29.29). Similarly, the intensities of diopside peaks between 30.42 and about 30.74° declined, suggesting sensitivity of this phase to the attack of a strong acid. Calcium removal and, as a result, partial dissociation of major binding phases led to the loss of the bond strength after 20 days of the samples exposure.

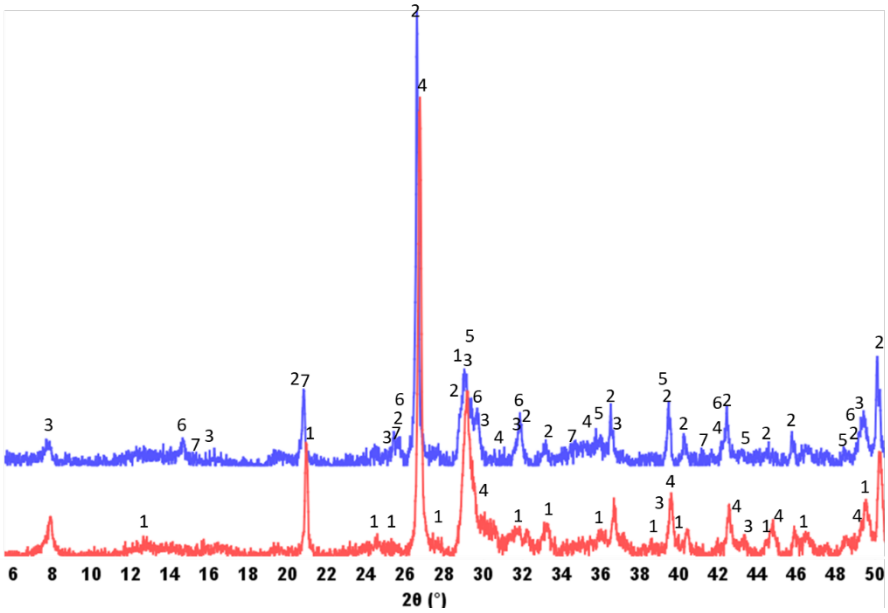

Figure 7. XRD patterns of GBFS/SiO_2 blend before (bottom) and after (top) the 30-day acid exposure. 1-xonotlite, 2-quartz, 3-tobermorite, 4-diopside, 5-calcite, 6-basanite, 7-millosevichite.

3.3.2. Elemental mapping – μEDX

The elemental mapping was performed on the samples exposed to the strong acid. Spatial coexistence of different elements may help elucidate the degradation mechanism through understanding of the reaction products between the cementitious material and the acidic environment. This was the case for samples with GBFS and OPC. However, in other cases, the elemental patterns cannot be easily interpreted; this was the case of TSRC samples exposed to the acid.

Figure 8 gives the elemental maps and the composition of the major oxides in TSRC covering CS plates after the acidic brine exposure tests.

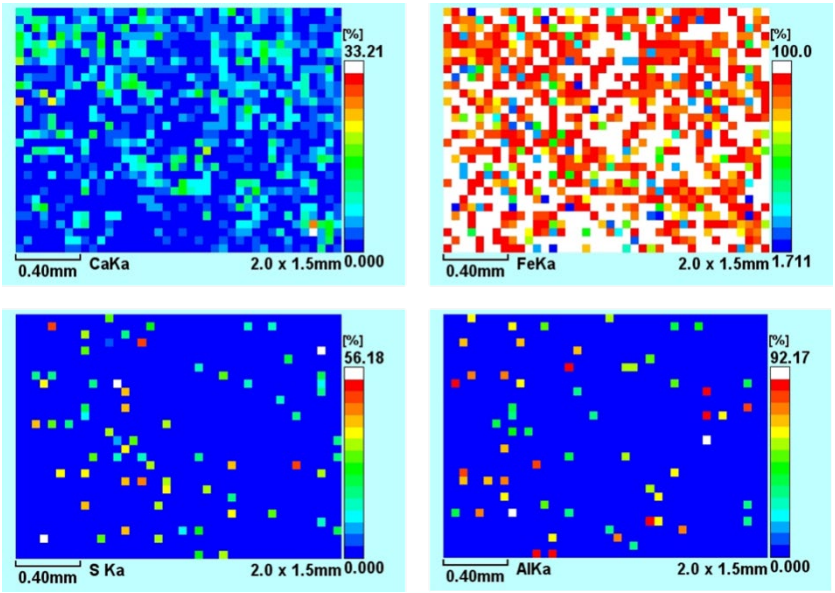

Oxide	Mass percent		
	Site-1 (shown above)	Site-2	Site-3
Al_2O_3	35	23	24
Fe_2O_3	29	40	38
SiO_2	23	22	22
SO_3	6.1	4.4	4.8
CaO	2.2	5.8	5.9

Figure 8. μEDX elemental maps and an oxide composition of the TSRC-covered CS samples after a 30-day exposure to H_2SO_4/brine solution at pH 0.6 and 90°C.

The color schemes give quantitative evaluations of individual elements, with the contents decreasing as the color changes from white (100% element) through red, yellow, and green colors to blue (0% element). Relating sulfur to other elements is not straight forward based on these results. There are no clearly overlaying sulfur-calcium signals (a high calcium content does not always match a high sulfur content in the maps).

In addition to calcium, the maps of sulfur correspond to iron and aluminum. The quantitative data (in the table) show higher sulfur for the sites with higher aluminum rather than with higher calcium or iron contents (site 1 vs. sites 2 and 3). Association of sulfur with aluminum could be interpreted as possible presence of aluminum sulfate or low amounts of crystalline Millosevichite (see section 3.3.1.). Presence of hydrated iron sulfate or anhydrate cannot be excluded.

The quantitative data (Figure 8) of oxide composition clearly suggest the depletion of calcium in the samples as a result of reaction with sulfate ions. Despite the calcium removal, there was still significant cement coverage of CS plates and the bond strength, although decreased, could be measured after 30 days of strong acid exposure. This indicates that some sodium-aluminum-silicate-based phases still ensured the bonding in the calcium-depleted cement.

The measurements of the GBFS/SiO_2 samples shown in Figure 9 suggest sulfur – calcium association. Both maps and the table show higher sulfur content at the locations of calcium accumulation. This result is in agreement with the XRD measurements that showed bassanite in the acid-exposed GBFS/SiO_2 covering CS plates. The silicon content is low in these samples, suggesting that after calcium removal through reaction with sulfates, silicon was washed out probably as a gel. This process resulted in a gradual loss of the original bond and CS corrosion.

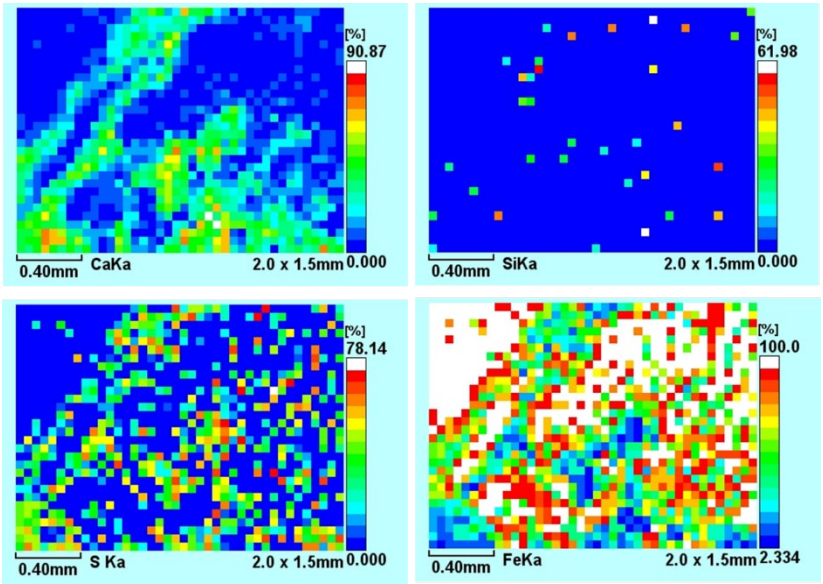

Oxide	Mass percent		
	Site-1 (shown above)	Site-2	Site-3
SO_3	34	40	19
Fe_2O_3	42	38	57
CaO	14	23	7
SiO_2	9.8	-	-

Figure 9. μEDX elemental maps and an oxide composition of the GBFS/SiO_2-covered CS samples after the 20-day exposure to H_2SO_4/brine solution at pH 0.6 and 90°C.

In the case of the OPC/SiO_2 covered CS plates (Figure 10), there was no/or very little sulfur associated with the cement, unlike for the TSRC and GBFS/SiO_2 samples. In fact, the original bond between the cement and CS was already weak. The samples survived only 18 days of the acidic brine exposure. At the end of this period, the interfacial bond failed with most of the cement staying on one of the plates. It is probable that calcium was just washed out sufficiently to lead to the bond failure. On the other hand, the maps of chlorine clearly show its association with calcium in the areas still covered by cement. The quantitative data show higher chlorine content at the sites with higher calcium. Formation of calcium silicate chloride hydrate (Rusinovite, ICDD 00-063-0365) cannot be excluded but it could not be confirmed by the XRD measurements with certainty because of the low content (if any) and complex XRD patterns with overlapping peaks of different minerals. The absence of sulfur in the cement agreed with the XRD data that did not show any noticeable peak of calcium sulfate.

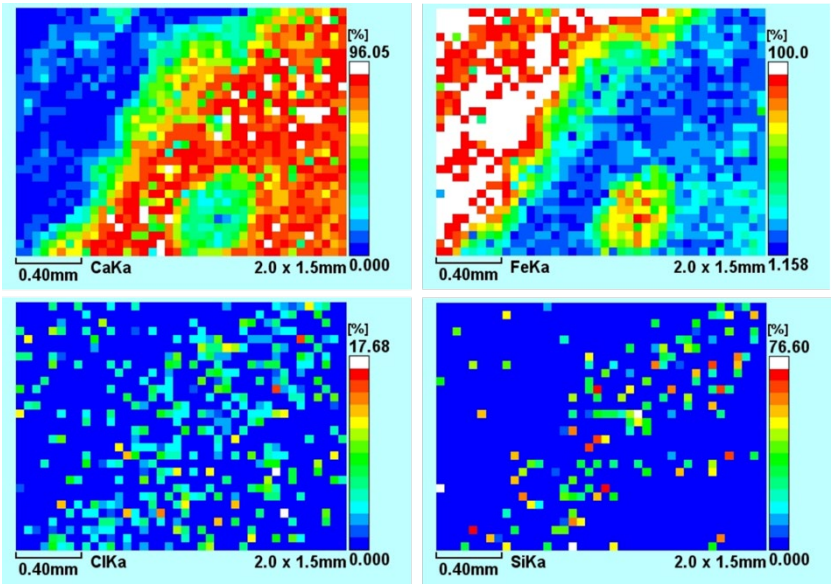

Oxide	Mass percent		
	Site-1-edge (shown above)	Site-2	Site-3
CaO	34	2.7	52
SiO_2	27	8.8	18
Fe_2O_3	34	88	16
Cl	1.4	0.6	2.3

Figure 10. μEDX elemental maps and an oxide composition of the class G/SiO_2-covered CS samples after the 18-day exposure to H_2SO_4/brine solution at pH 0.6 and 90°C.

3.3.3. ATR-FTIR analyses

To support the information obtained from the XRD study, ATR-FTIR analysis was carried out for the cement samples covering CS surfaces before and after the acidic brine exposure tests. Figure 11 shows the ATR-FTIR absorption spectra in the region from 2000 to 670 cm^{-1} for TSRC, OPC, and GBFS cements before the exposure. As described in our previous paper (T. Pyatina et al. 2016), the contributors to these absorption bands included the following five groups: water, carbonate, sulfate, silicate, and silica. The band at 1638 cm^{-1} was the H-O-H bending ($\delta_{H\text{-}O\text{-}H}$) in water. The carbonate group, CO_3^{2-}, was represented by 1489, 1452, and 1418 cm^{-1} bands attributed to the C-O anti-symmetrical ($V_{asC\text{-}O}$) stretching vibration in CO_3^{2-} and correspondingly, the band at 877 cm^{-1} belonged to O-C-O out-of-plane bending ($\delta_{O\text{-}C\text{-}O}$) in CO_3^{2-}. The presence of amorphous silica was identified by the bands at 1245 and 1204 cm^{-1}, while the crystalline silica as quartz gave the bands at 1077 cm^{-1} assigned to Si-O anti-symmetric ($V_{asSi\text{-}O}$) and at 799, 779, and 669 cm^{-1} corresponding to the symmetric ($V_{sSi\text{-}O}$) stretching vibrations. There were two different types of silicate. One was calcium silicate hydrates (C-S-H) formed in class G/SiO_2 and slag/SiO_2 cements; the other was sodium, calcium aluminosilicate hydrate (N,C-A-S-H) and sodium aluminosilicate hydrate (N-A-S-H) formed in the TSRC. For the former cements, the C-S-H-related Si-O anti-symmetric stretching ($V_{asSi\text{-}O}$) in silicate SiO_4^{-4} can be recognized by the presence of the principal band at 965 cm^{-1}. For the latter, the principal peak at 983 and a shoulder peak at 901 cm^{-1}, respectively, were assigned to the M-O (M: Si or Al) anti-symmetric ($V_{asM\text{-}O}$) stretching mode in the Na^+-O-Ca-O-Si-O-Al and Na^+-O-Si-O-Al linkages related to amorphous- or crystalline-N,C-A-S-H and –N-A-S-H silicate reaction products. On the other hand, the sulfate group was associated with the band at 1156 cm^{-1} corresponding to the S-O symmetric stretching ($V_{s\,S\text{-}O}$) in the SO_4^{2-}-related compounds.

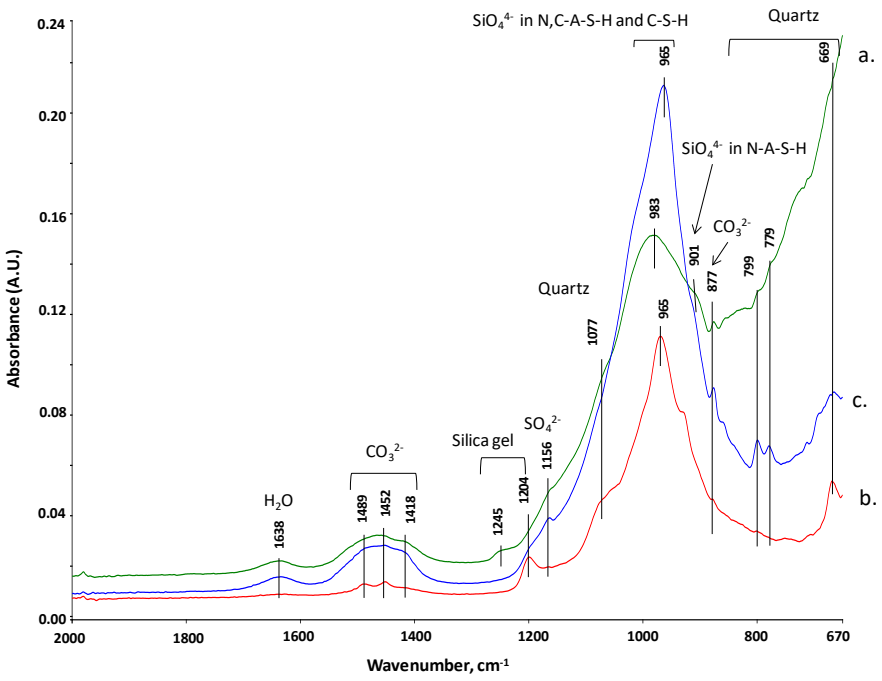

Figure 11. ATR-FTIR absorption spectra of TSRC (a), OPC/SiO_2 (b), and GBFS/SiO_2 (c) cements adhering to CS before the acid exposure test.

Figure 12 illustrates ATR-FTIR spectra for cements remaining on the CS surfaces after the acid-corrosion and –erosion damages of the cement/CS joints. For the TSRC, there were three changes in the spectral features of the acid-damaged cement. Firstly, V_{as}M-O stretching at 901 cm^{-1} attributed to N-A-S-H became the major band, while N,C-A-S-H-related V_{as}M-O at 983 cm^{-1} became secondary. This result strongly suggested that amorphous and crystalline sodium-aluminum-silicate hydrates not only acted to impede acid erosion of cement adhering to CS, but also offered an improved interfacial bond durability of cement to CS in the acid environment; secondly, the peak intensity of carbonate-related bands was considerably reduced, implying that the carbonate compounds formed in this cement were susceptible to the acid erosion; and thirdly, the additional silica gel was produced. It should be noted that the peak intensity of sulfate-related bands did not significantly increase after the acid exposure tests, which means that if sulfate reaction products formed, their amounts were small.

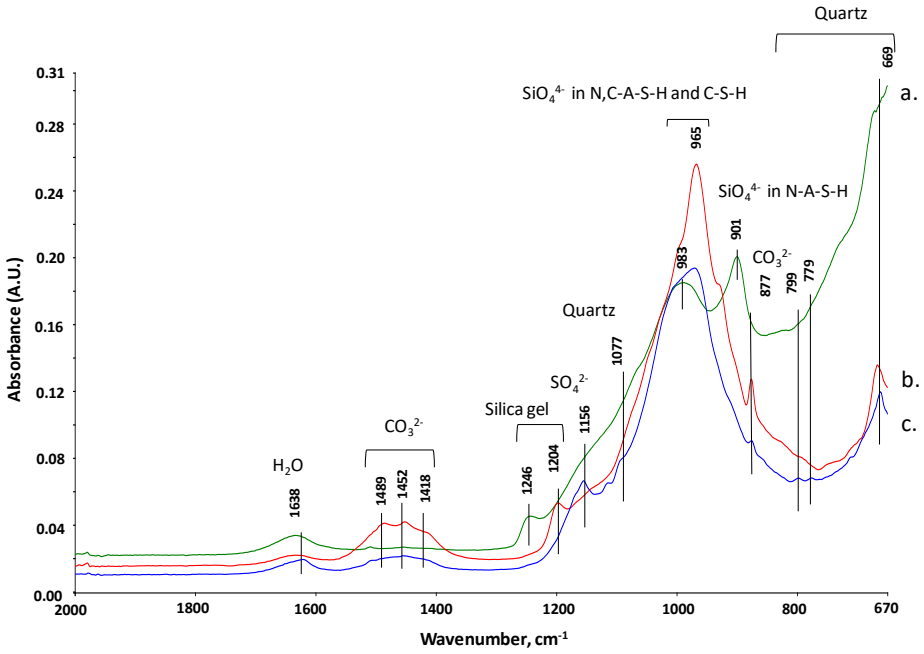

Figure 12. ATR-FTIR absorption spectra of TSRC (a), OPC/SiO_2 (b), and GBFS/SiO_2 (c) cements present at corroded and eroded cement/CS interface after the acid exposure tests.

For the eroded OPC/SiO_2, the major changes for samples after the acid exposure was visible in the three reaction products: carbonates, silica gels, and the C-S-H phases. There was no evidence whether carbonation reactions of the eroded cement took place during the acid exposure or during the drying of eroded cement in an air oven at 90°C. Furthermore, the C-S-H compounds as the major hydrate phase were further formed in cement during the acid exposure. Like the TSRC, the formation of sulfate reaction products was very small, if any.

For the eroded GBFS/SiO_2, unlike for the TSRC and the OPC, two specific changes for the acid exposed sample were noticeable. One was the ascent of a sulfate-related band intensity, corresponding to the increase in sulfate reaction products; the other was the decline in the quartz content. There was no significant change in the peak intensity at 983 cm^{-1} attributed to C-S-H phases.

There was a general agreement between the ATR-FTIR, XRD and μEDX mapping data on the composition of acid-exposed samples. In particular, ATR-FTIR confirmed the increase of sodium-aluminum-silicate hydrates in the TSRC, a further formation of calcium-silicate hydrates in the OPC/SiO_2 and the sulfates presence in the GBFS/SiO_2 specimens after the exposure.

3.3.4. Raman imaging

The Raman imaging was done on control samples after a day curing at 300°C and samples exposed to the acidic brine after 30 days for TSRC-, 20 days for GBFS/SiO_2- and 18 days for OPC/SiO_2 samples. An effort was made to select representative areas for the analysis. Three maps were registered for each sample. However, due to the high degree of non-homogeneity of the samples and limited map areas, the integrated information that could be obtained with this method was limited. The TSRC samples (not shown) were strongly luminescent without clear peaks that could allow phase identification, likely due to the low crystallinity of these samples.

The GBFS (Slag)/SiO_2 and the OPC (G)/SiO_2 control and acid-exposed samples' images are shown in Figure 13. The maps of tobermorite were made based on the major peak at 660 cm^{-1} and those of sulfate based on their major peak at 115 cm^{-1}. The images of the control and treated GBFS/SiO_2

were strikingly different. The control sample surface composition was clearly dominated by tobermorite, while the signal from the sulfate was at the level of a background. The acid-exposed one was totally dominated by the sulfate products, and the tobermorite became a minor component of the cement composition. This result agrees with the XRD, μEDX and ATR-FTIR studies that suggested sulfate reaction with the GBFS-based cement and sulfates accumulation. The XRD data suggested the presence of bassanite in the samples.

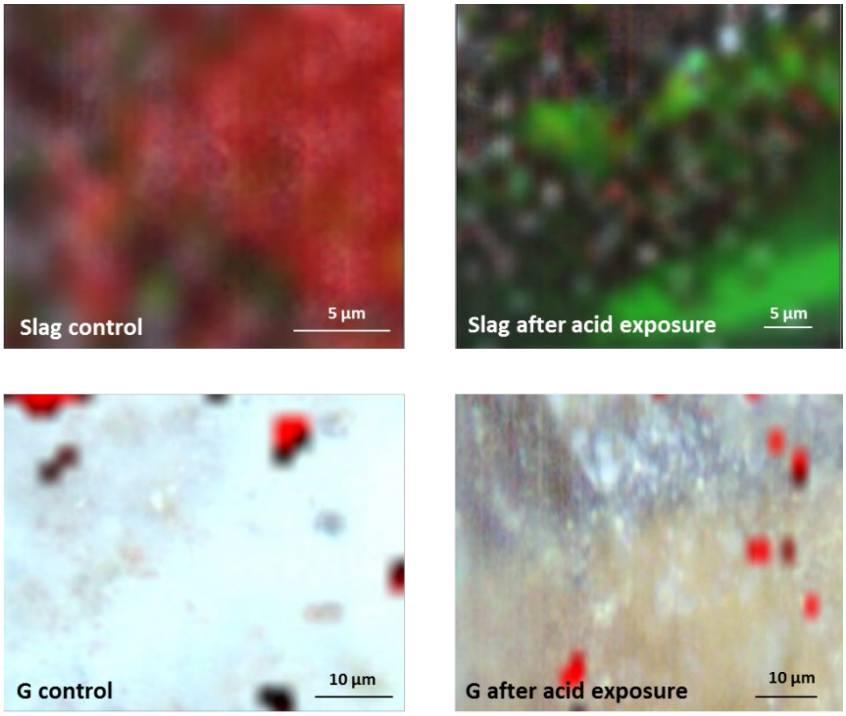

Figure 13. Raman maps of the GBFS (Slag)/SiO_2 and the OPC (G)/SiO_2 samples before and after the acid/brine solution exposure at 90°C for 20 and 18 days respectively. The red color in the GBFS/SiO_2 map shows tobermorite (660 cm^{-1}) and the green color sulfate peaks (115 cm^{-1}) intensities. The red color in the OPC/SiO_2 samples shows intensities of sulfate peaks.

The experimental data on cement-steel bond durability under the thermal shock and acidic brine environments and corrosion protection of CS by the tested composites at early autoclaving age clearly verified that among the alkali-activated composites, the TSRC showed the best performance in improving bond durability and minimizing corrosion of CS. Thus, the TSRC was selected to conduct further studies regarding the effect of MGF on self-re-adhering to CS and its protection from corrosion by the self-re-adhered composite for samples after 30-day-long autoclaving at 300°C before the bond damage. In this study, the Class G/SiO_2 composite was used as a reference.

3.4. Susceptibility of MGF to reactions with alkali-activated cement pore solution at 300°C

To verify whether the MGF are susceptible to alkaline attack of the TSRC slurries, the MGF was mixed with the pore solution separated by a centrifuge from the TSRC slurry 10-minutes after the slurry mixing. The fibers were covered with the pore solution, mixed and autoclaved for 24 hrs at 300°C. The autoclaved paste solidified as a result of fiber-alkali pore solution reactions. The crystalline phase composition of the MGF-pore solution reaction products determined by XRD is summarized in Table 2. There were three major crystalline phases, silica in the form of coesite, zeolite analcime, and Al-substituted tobermorite. The test confirmed MGF's susceptibility to the TSRC pore

529 solution and possibility of MGF contributing to the formation of the phases that participate in the
530 healing of the damaged TSRC (Pyatina and Sugama 2020) through MGF high-temperature alkaline
531 degradation.
532
533 **Table 2**. Crystalline phases formed by MGF in the TSRC pore solution after autoclaving for 24hrs at 300°C.

ICDD number	Major phases	Semi-quantitative evaluation
01-075-8689	Analcime, $Na_{1.71}((Al_{1.806}Si_{4.194})O_{12})(H_2O)_{2.16}$	40
04-015-7162	Coesite, SiO_2	29
01-074-2878	Tobermorite, aluminum $Ca_{4.9}(Si_{5.5}Al_{0.5})_{16.3})(OH)_{0.7}(H_2O)_{0.5}$	19
01-077-8366	Tobermorite 11A $Ca_4(Si_6O_{15})(OH)_2(H_2O)_5$	9
01-082-3579	Aklimaite $Ca_4(Si_2O_5(OH)_2)(OH)_4(H_2O)_5$	3

534

535 *3.5. Self-re-adhering properties of the 30-day autoclaved sheath composites*

536
537 In this work, the self-re-adhering properties of the 30-day autoclaved TSRC/MGF composite
538 sheath and the two reference composites, the OPC/SiO_2 and the TSRC without MGF, were evaluated.
539 All composites were prepared by autoclaving for 30 days in 300°C. Figure 14 compares the sheath-
540 shear bond strengths of 1- and 30-day-autoclaved sheath samples before and after the re-adherence
541 for 5 days in water at 300°C. For the 1-day autoclaved samples, the bond strength of the MGF-free
542 reference samples, the OPC/SiO_2 and the TSRC, was 0.23 and 0.51 MPa, respectively. Compared with
543 these strength values, incorporation of MGF offered a significant increase in the bond strength to 1.35
544 MPa, highlighting that the fast dissolution and reactions of MGF improved the bond strength in the
545 critical interfacial boundary regions between a cement sheath and CS. All 30-day-autoclaved
546 composites demonstrated increased bond strength, compared with that of 1-day-autoclaved ones.
547 The value of the 30-day sheath-shear bond strength was 0.48 MPa for OPC/SiO_2, 0.57 MPa for TSRC,
548 and 1.69 MPa for TSRC/MGF, which is tantamount to 2.1-, 1.1-, and 1.3-fold rise in the bond strength,
549 respectively, over the 1-day bond strength. However, one concern for the TSRC/MGF composite was
550 the excessive sheath shear bond strength of nearly 1.7 MPa, thereby resulting in the development of
551 undesirable multi-radial cracks in the sheath during the shear stress-debonding process (the photo
552 in Figure 14). Such crack development resulted in a low rate (28%) of the bond recovery, implying
553 that the re-adhering treatment of 5 days may be insufficient in achieving an adequate re-adherence
554 of the radially cracked composite. In contrast, there were no visual cracks on the other two reference
555 composites after the bond testing. This fact suggested that a sheath bond of moderate strength may
556 be required to provide interfacial bond toughness of the composite adhering to CS, rather than the
557 development of excessive bond strength with a brittle adhesive nature leading to the formation of
558 visible perpendicular cracks in the composite sheath.
559 Overall, MGF-free TSRC exhibited the best bond recovery performance of 49% and 57 % for the
560 1-day- and 30-day-autoclaved composites, respectively. On the other hand, the bond recovery of the
561 30-day-autoclaved OPC/SiO_2 reference sample was only 38%.
562

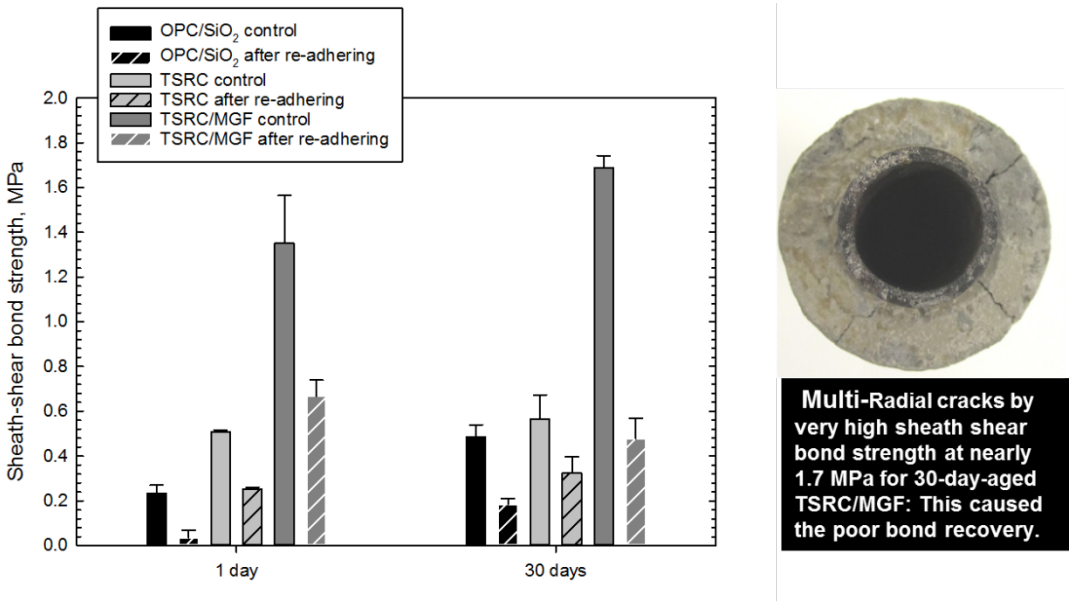

Figure 14. Sheath-shear bond strength of the 1- and 30-day-acutoclaved TSRC/MGF composite sheath, and MGF-free TSRC and OPC/SiO_2 reference composite sheaths before and after the self-re-adherence 5-day treatment at 300°C.

3.6. Corrosion mitigation of CS by self-re-adhered composites

After the debonding of the composite sheath from CS, the remaining composite layer must protect the CS from corrosion and this protection must improve after the self-re-adherence treatment. We evaluated whether additional composite layers that deposit on the CS during the re-adhering period further enhance its corrosion protection. To obtain this information, the CS plate /composite adhesive/CS plate lap joint samples were prepared by autoclaving them in 24-hrs-300°C plain water. In this work, two composites (TSRC and OPC/SiO_2) modified and unmodified with MGF were employed, and their ability to inhibit corrosion of CS was evaluated for a composite layer adhering to CS surfaces after the 1st and 2nd lap-shear bond tests by DC electrochemical polarization in brine. As described in the section 2.3. "Samples preparation", after the 1st bond strength test, two debonded CS plates were reattached by steel wire (Figure 15), and then the reattached plate samples were autoclaved for 5 days in plain water at 300°C. After the autoclaving, the 2nd time bond strength test was conducted, and thereafter the plate with the thinner composite layer was further tested to obtain quantitative corrosion-related data showing whether the re-adherence treatment improved corrosion protection of CS. The data included the corrosion rate of CS, the coverage of CS by the composite, and cathodic corrosion protection by the composite. The electrochemical corrosion-related data were collected from DC potentiodynamic polarization curves (Figure 15). As was mentioned above, we selected the CS site covered with a thinner composite layer. The results were the average of the data obtained from three different locations of cement-covered CS samples. On the polarization curve, the corrosion potential denoted as E_{corr} accounts for the extent of cement's coverage over CS; a high value of E_{corr} means a better coverage with a minimum spacing between the composite and CS. The corrosion current density marked as I_{corr} provides information on the protection from the cathodic corrosion: $H_2O + 1/2O_2 + 2e^- \rightarrow 2OH$; a low I_{corr} value means a minimum permeation of water and oxygen through cement layer covering CS surfaces. In other words, a cement layer with low I_{corr} is dense, with a low water and oxygen permeability.

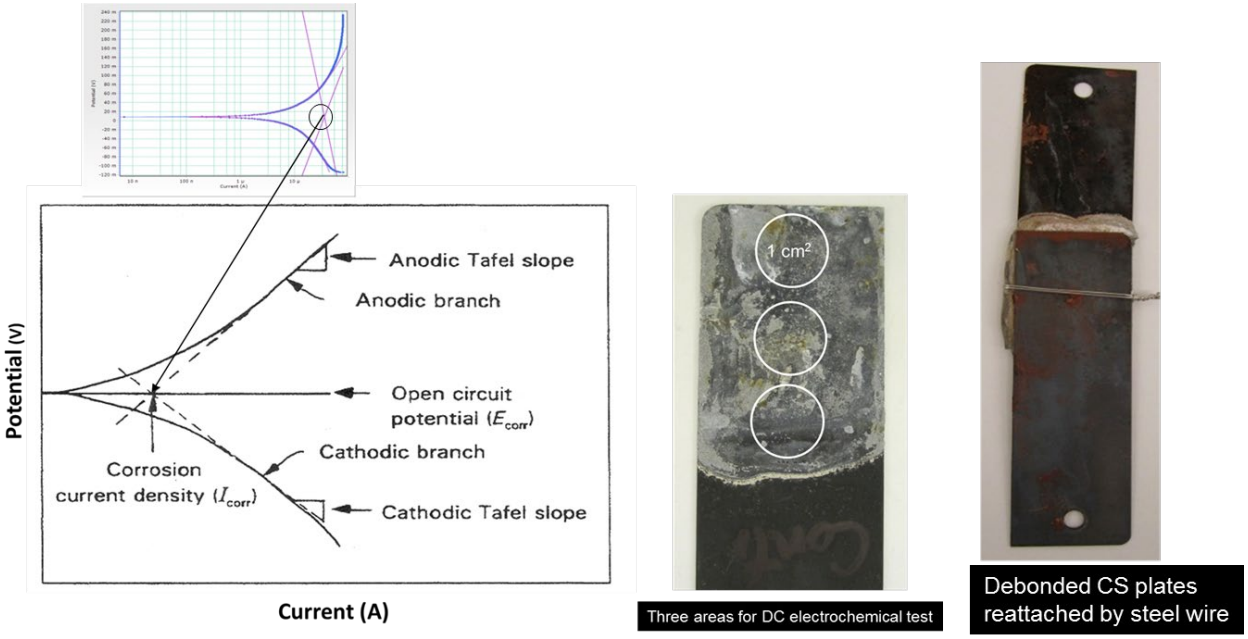

Figure 15. The DC electrochemical potentiodynamic cathodic-anodic polarization diagram for a composite-covered CS after a lap-shear bond test.

Figure 16 depicts the average E_{corr} and I_{corr} values for CS plates covered with the OPC/SiO_2 and TSRC composite layers modified and unmodified with MGF. The obtained E_{corr} and I_{corr} data correlated with the thickness of the composite layers covering the CS surfaces and the corrosion rate of underlying CS. The corrosion rate was computed based on several parameters including E_{corr} and I_{corr} values in the polarization curves. The unmodified TSRC exhibited the best coverage over the CS surface, reflecting the highest E_{corr} of +14 mV, while the CS without any coverage had the lowest E_{corr} of -185 mV. The relatively moderate coverage in the range from ±0 to -50 mV was detected for both MGF-modified OPC/SiO_2 and TSRC, underscoring that MGF contributed to the moderate coverage for all composites. Relating this finding to the results of the lap-shear bond strength tests, such good coverage resulted from the increased adhesive force of composite-modified with MGF to CS. Furthermore, the MGF also helped in impeding cathodic corrosion reactions of CS; in fact, the I_{corr} value was the lowest with MGF, especially, the OPC/SiO_2 indicated a considerable reduction of this value. Since the lowering of I_{corr} value implies low permeability of oxygen and water as corrosion initiators through composite layer, it is possible to assume that MGF offered the densified composite structure. Addition of MGF resulted in higher E_{corr} in comparison with the non-modified TSRC samples. However, MGF decreased corrosion current and increased the thickness of the composite layer.

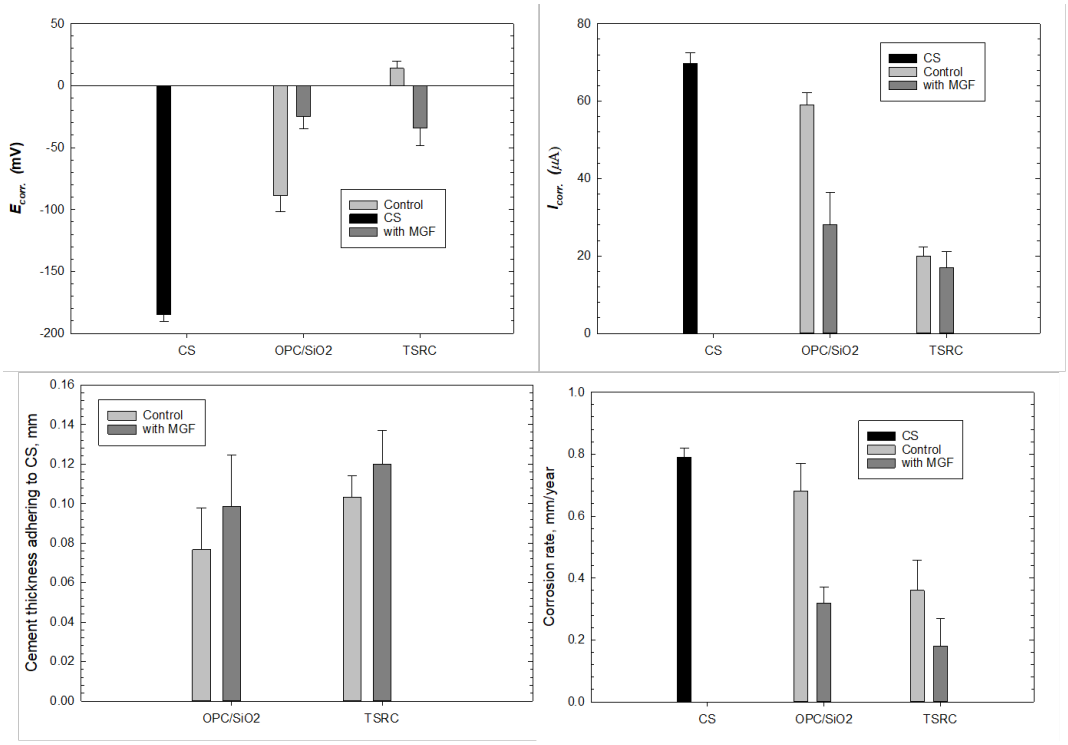

Figure 16. Comparison of E_{corr}, I_{corr}, and the composite CS coverage thickness affecting the corrosion mitigation of CS by the MGF-modified and unmodified OPC/SiO_2 and TSRC composites.

The thickness of the composite layer remaining on CS was 0.07 mm for the OPC/SiO_2 and 0.10 mm for the TSRC composites; this thickness increased by 28% and 17% respectively with the MGF.

Corrosion rates were calculated based on cathodic and anodic Tafel slopes, corrosion current density, corrosion potential and CS properties (Stern and Geary 1975). Without MGF, the corrosion rate of CS protected by the OPC/SiO_2 was 0.68 mm/year. This corrosion rate was nearly 2-fold lower, 0.36 mm/year, for the TSRC covered CS. The incorporation of MGF led to a considerable reduction of the corrosion rate to 0.32 mm/year for OPC/SiO_2 and to 0.18 mm/year for TSRC.

Using the samples tested for corrosion, we evaluated the ability of the re-adhered composites to further mitigate the corrosion of CS. As described earlier, the two debonded CS plates were reattached with a wire, and then exposed to plain water at 300°C for 5 days as re-adherence treatment. Afterward, the re-adhered plates were again tested in lap-shear bond tests. It should be noted that the shear bond strength of the re-adhered plates was too weak to be measured. Nonetheless, after the 2nd time lap-shear bond test, the same CS side as the one tested after the 1st lap-bond test was examined to obtain information on the corrosion protection by the self-re-adhered composites. Since relatively large amounts of TSRC remained on the two cohesively debonded CS plates, these plates reattached through the composite-to-composite bonding during the re-adherence treatment.

Figure 17 compares the representative polarization curves of CS protected with the OPC/SiO_2 composite modified and non-modified with MGF and the appearance of the debonded CS before and after the re-adherence to CS. For the unmodified OPC/SiO_2 composite the re-adherence treatment did not change significantly the average values of E_{corr} and I_{corr}. The noticeable changes in the E_{corr} value from -25 mV "before" to 6 mV "after" were observed for the MGF-modified composite, implying that MGF acted to improve the coverage of the composite over the CS surface during the re-adherence treatment. Meanwhile, the I_{corr} value somewhat increased from 28 μA to 74 μA during the treatment, suggesting that water and oxygen permeability of the re-adhered composite increased. Overall, more corrosion stains were generated beneath all the re-adhered composite layers of OPC/SiO_2.

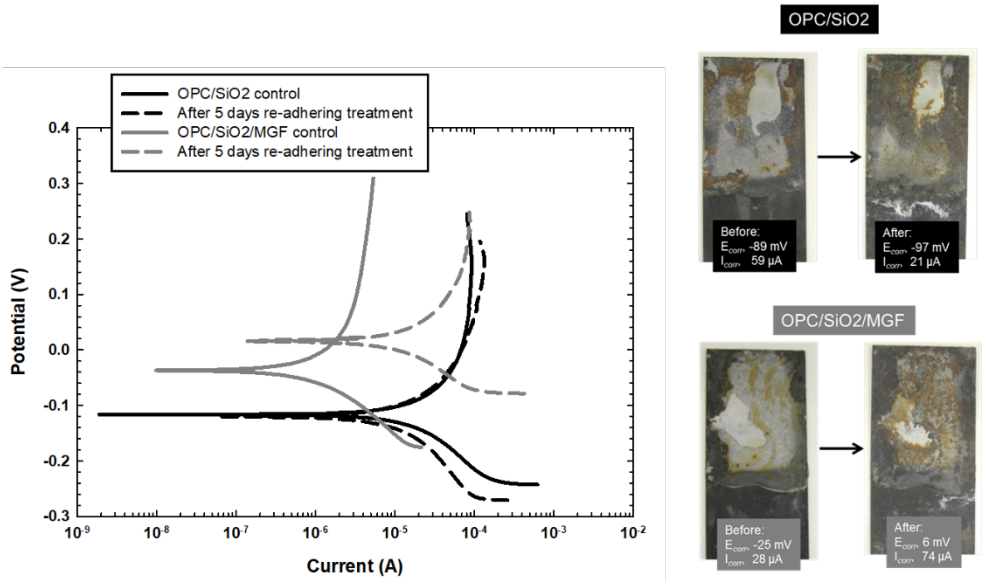

Figure 17. Polarization curves and appearances of the debonded CS surfaces for the MGF-modified and non-modified OPC/SiO_2 composites before and after the self-re-adherence treatment.

In the case of TSRC, there was less corrosion of the underlying CS than for the OPC/SiO_2 composite; correspondingly, a new re-adhered composite layer superimposed on the pre-existing composite layer was visible (Figure 18). For non-modified TSRC, the E_{corr} value significantly increased by 8.4-fold from 14 mV to 118 mV after the re-adherence, emphasizing that the re-adherence treatment provided the improved coverage of CS by the composite, while I_{corr} decreased. For the re-adhered MGF-modified TSRC, E_{corr} value increased from -83 mV to -34 mV due to the improved coverage after the re-adherence treatment. The corrosion current value increased to 41 µA, indicating a reduced cathodic corrosion protection. However, this value was still lower than for MGF-modified OPC/SiO_2.

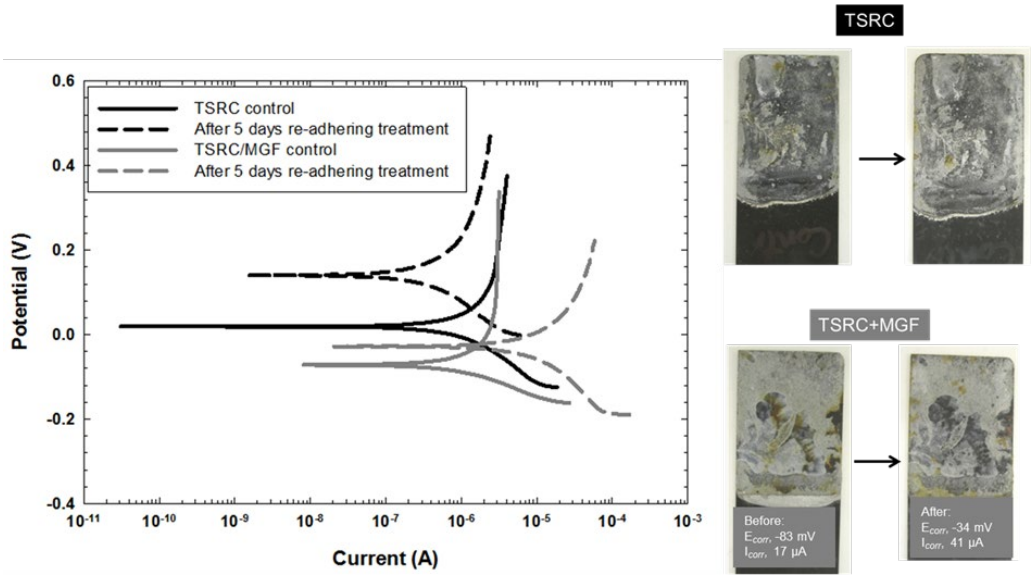

Figure 18. Polarization curves and an appearance of the debonded CS surface for the MGF-modified and unmodified TSRC adhesives before and after the re-adherence treatment.

Figure 19 represents the thicknesses and corrosion rates of CS covered with the MGF-modified and non-modified composites before and after the re-adherence treatment. The MGF-modified and non-modified TSRC showed a considerable increase in thickness of composite layers after the re-

adherence. In fact, the thickness of both MGF-modified and non-modified TSRC rose by nearly 2.3-times after the treatment. The MGF also assisted in increasing the thickness of OPC/SiO_2, but not as much as for TSRC. Thus, the effect of MGF in alkali-activated TSRC composite on self-re-adhering performance was stronger than that in the OPC/SiO_2 composite.

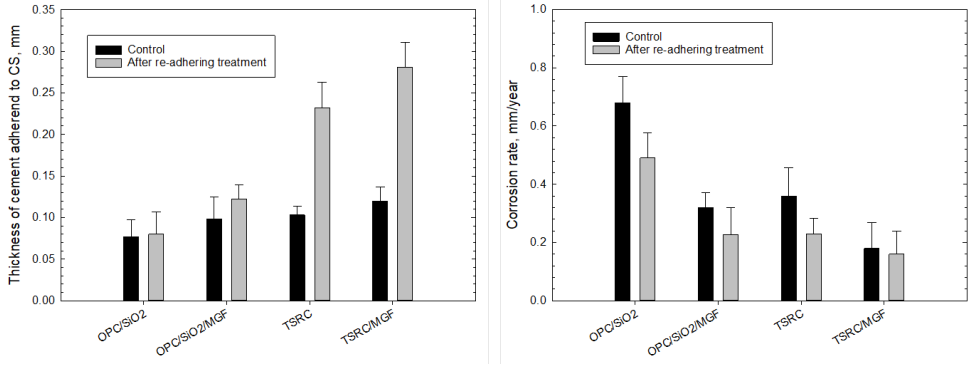

Figure 19. The thickness of the composite adhesives on the corrosion rate of CS protected by the MGF-modified and non-modified OPC/SiO_2 and TSRC composites before and after the re-adherence treatment.

Both non-modified OPC/SiO_2 and the TSRC composites improved the overall corrosion protection of CS after the re-adherence treatment (Figure 19). The corrosion rates of 0.49 and 0.23 mm/year for the OPC/SiO_2 and TSRC were reduced by 28% and 36% compared with those before the treatment. Further corrosion mitigation was observed from the re-adhered MGF-modified OPC/SiO_2 and TSRC, reflecting the corrosion rate of 0.23 and 0.16 mm/year, respectively. The additional composite coverage superimposed on the pre-existing composite layer by the re-adherence treatment appeared to further improve the corrosion protection of CS.

Furthermore, we investigated the CS corrosion protection by the 30-day-autoclaved MGF-modified TSRC. In this work, two non-modified reference composites, OPC/SiO_2 and TSRC, were used for comparison. TSRC and TSRC/MGF provided an ideal coverage of CS surfaces; namely, the entire lap-joint areas of both CS plates were covered with these composites and the bond failed cohesively (Figure 20). The CS coverage by the composite after the 30-day autoclaving was clearly much greater than after a day of autoclaving, corresponding to nearly 2.4-fold increased thickness (Figure 20). Similarly, the increased thickness was observed for the 30-day-autoclaved OPC/SiO_2. However, one concern was the Fe-related corrosion product, magnetite (Fe_3O_4), which formed dark spots in the areas of CS not covered by the composite. Magnetite is soluble in acids, so although it may slow down water-corrosion of CS it cannot protect it under acidic environments. As expected, the increased coverage resulted in the reduction of corrosion rate (Figure 20). In fact, compared with that of the 1-day-autoclved samples, the corrosion rate of 30-day autoclaved CS protected by the composites reduced from 0.18 to 0.16 mm/year for TSRC/MGF, from 0.36 to 0.25 mm/year for TSRC, and from 0.68 to 0.59 mm/year for OPC/SiO_2.

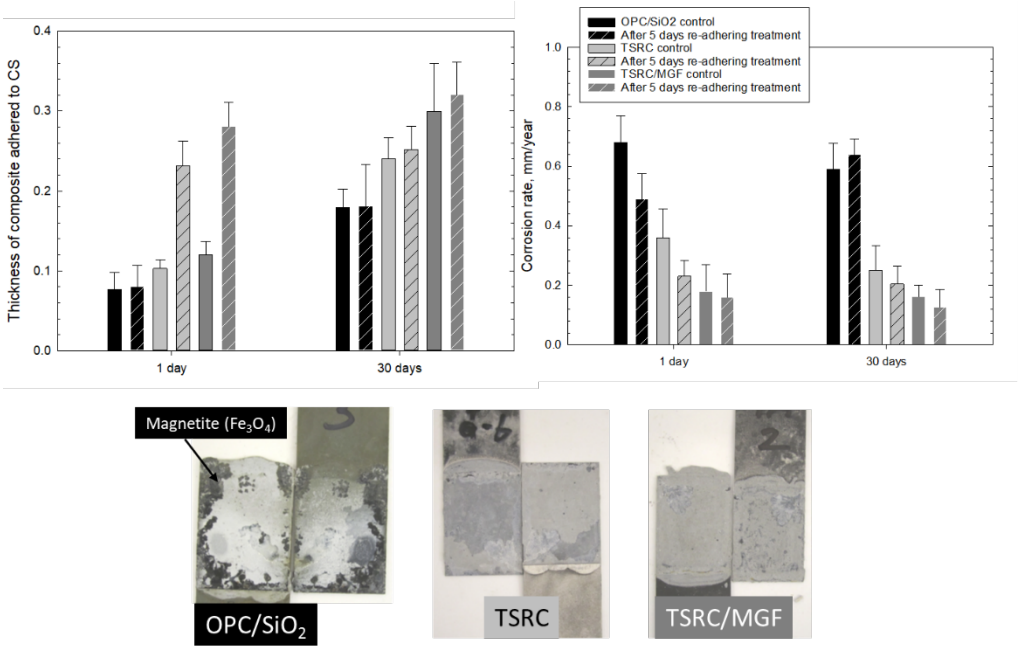

Figure 20. The thickness of the composite adhesive at CS surfaces, corrosion rate of CS, and an appearance of the debonded CS sites for 300°C-30-day-autoclaved MGF-modified and non-modified TSRC and OPC/SiO_2 composites.

After the re-adherence treatment, the thickness of the re-adhered 30-day-autocalved TSRC/MGF and TSRC composites over CS somewhat increased to 0.32 mm from 0.28 mm and to 0.25 mm from 0.23 mm, respectively with a corresponding decrease in the corrosion rate to 0.13 mm/year for TSRC/MGF and 0.2 mm/year for TSRC. Hence, after the interfacial debonding for the 30-day-aged TSRC/MGF and TSRC composites, the composites remaining on the CS surface provided an excellent corrosion protection of CS against brine-caused corrosion, which further improved after the additional 5 days at 300°C. By contrast, the OPC/SiO_2 showed no signs of the changes in the composite layer thickness after the re-adherence treatment, and there was no enhancement of corrosion impediment, rather the corrosion rate increased from 0.59 to 0.64 mm/year after the re-adherence treatment.

The integrated information of all adhesion- and corrosion-related data described above strongly verified that the adequate corrosion protection of CS was essentially governed by the following two principal factors: good wetting and spreading behavior of composite slurries over CS surfaces, reflecting uniform coverage by the composite layer; and an outstanding adhesive behavior of composite to CS, leading to the development of high interfacial bond strength between the composite and CS and cohesive bond failure when damaged. From this point of view, the alkali-activated TSRC/MGF demonstrated the best wetting and adhesive behaviors to CS, while such behaviors of non-activated OPC/SiO_2 were relatively poor.

4. Conclusions

Based on the experimental information on composites' adhesive behaviors, interfacial bond durability, self-re-adhering performance, and corrosion protection of CS before and after the self-re-adhering treatment, the following conclusions can be drawn.

1. For the short-term (1 day)-300°C autoclaved TSRC, GBFS/SiO_2, FAC/FAF and OPC/SiO_2 composites adhering to CS, the first two alkali-activated composites failed cohesively with the locus of the bond failure being in the composite itself and not at the critical composite-CS interfacial region. The FAC/FAF and OPC/SiO_2 failure mode was mixed, both the adhesive and cohesive failures. The lap-shear bond strength for the first three composites was much greater (> 1.2 MPa), than for OPC/SiO_2 (0.4 MPa).
2. The bond durability of these composites was evaluated under two different stress environments, in 6 cycles of thermal shock stresses and a 30 day-acid. TSRC significantly

outperformed the other tested composites under both environments. After the thermal shock, the sheath-shear bond strength of TSRC reduced by 51% to 0.25 MPa. By contrast, the OPC/SiO_2 composite strikingly lost the bond strength that dropped from 0.23 MPa before to 0.05 MPa after the thermal shock, while the GBFS/SiO_2 sheath failed catastrophically in the first thermal shock cycle. In the acidic brine environment, the most of the OPC/SiO_2 adhesive layer eroded after an exposure of 18 days, engendering a catastrophic interfacial bond failure. The acid erosion was minor for GBFS/SiO_2; instead, the acid treatment removed calcium from calcium-silicate hydrates, leading to the silicon-containing phases transforming into silica gel and the bond failure after 20 days of exposure. In contrast, the TSRC adhesive remained intact for the 30 days of the exposure with the persisting lap-shear bond strength of 0.55 MPa. The reason for this was the presence of crystalline and amorphous phases in sodium aluminosilicate-based reaction products that helped preserve cement/CS bond in a pH 0.6 acid/brine at 90°C for 30 days after calcium depletion.

3. The MGF, tested as a self-re-adhering aid, was susceptible to the alkaline attack of TSRC pore solution during autoclaving at 300°C for 24 hours, forming solid phases that participated in the composite-CS interfacial bond.
4. For 1-day 300°C-autoclaved samples MGF offered a striking increase in bond strength of TSRC to 1.35 MPa, corresponding to 2.7-fold higher than that of the MGF-free TSRC through dissolution and reactions of MGF under the experimental conditions. The bond strength further increased to 1.69 and 0.57 MPa with and without MGF, respectively after extended 30-day curing time at 300°C. However, such a high bond strength resulted in the development of undesirable multi-radial perpendicular cracks in the sheath during the shear stress-debonding testing of unconfined sheath samples. The developed cracks were responsible for the low rate (28%) of the bond recovery after the 5-day re-adherence tests, implying that re-adhering treatment of 5 days may not be enough to achieve an appropriate re-adherence of the composite. In contrast, there were no visual cracks in the MGF-free TSRC after the bond testing. This fact suggests that a moderate sheath bond strength may be preferable to provide a desirable interfacial bond toughness of composite adhering to CS, rather than the excessive bond strength with a brittle adhesive nature.
5. The composites' CS corrosion-protection behavior evaluated before and after the re-adherence treatment varied significantly with the nature of the composites. The CS's corrosion rate protected by non-modified TSRC composite was 0.36 mm/year, which was nearly two times lower than that of OPC/SiO_2. The incorporation of MGF reduced the corrosion rate to 0.18 mm/year. The re-adherence treatment of debonded TSRC/MGF composite further reduced corrosion rate to 0.16 mm/year. The extended initial autoclaving period of 30 days for the TSRC/MGF composite increased the thickness of the composite layer on CS by 2.4 times in comparison with the 1-day initial autoclaving, thereby resulting in a better mitigation of the corrosion. Furthermore, after the re-adhering treatment, the thickness of the re-adhered composite rose to 0.32 mm from 0.28 mm before the re-adhering and brought about a further reduced corrosion rate of 0.13 mm/year. Thus, although the interfacial debonding for a 30-day-aged composites occurred, the aged debonded composites still had self-re-adhering capability and improved corrosion mitigation. By contrast, OPC/SiO_2 not only showed no change in thickness after the re-adhering treatment, but also the corrosion rate increased from 0.59 to 0.64 mm/year after the re-adherence treatment for this composite. Overall, the adequate corrosion protection of CS was essentially governed by the good wetting and spreading behaviors of composite slurries over CS surfaces, reflecting uniform coverage of steel with a composite layer and by an outstanding adhesive performance of a composite to CS, leading to the development of high interfacial bond strength between the composite and the CS. The alkali-activated TSRC/MGF revealed the best wetting and adhesive behaviors with CS, while such behaviors of OPC/SiO_2 were relatively poor.

5. Acknowledgements

This publication was based on the work supported by the Geothermal Technologies Office in the US Department of Energy (DOE) Office of Energy Efficiency and Renewable Energy (EERE), under the auspices of the US DOE, Washington, DC, under contract No. DE-AC02-98CH 10886. Raman data were acquired in SoMAS' Nano-Raman Molecular Imaging Laboratory (NARMIL), a community facility dedicated to environmental sciences' applications and founded with NSF-MRI grant OCE-1336724. Research was carried out in part at the Center for Functional Nanomaterials, Brookhaven National Laboratory, which is supported by the US Department of Energy, Office of Basic Energy Sciences, under Contract No. DE-SC0012704.

References

Alexander, K. M. 1960. "Reactivity of Ultrafine Powders Produced from Siliceous Rocks." *Journal of American Concrete Institute* 57:557–69.

Amin, M. N., J. S. Kim, Y. Lee, and J. K. Kim. 2009. "Simulation of the Thermal Stress in Mass Concrete Using a Thermal Stress Measuring Device." *Cement and Concrete Research* 39:154–64.

Kaldal, Gunnar Skulason, Magnus T. Jonsson, Halldor Palsson, and Sigrun N. Karlsdottir. 2016. "Structural Modeling of the Casings in the IDDP-1 Well: Load History Analysis." *Geothermics* 62:1–11.

Kaldal, Gunnar Skulason, Magnus Thor Jonsson, Halldor Palsson, and Sigrun Nanna Karlsdottir. 2015. "Structural Analysis of Casings in High Temperature Geothermal Wells in Iceland." *World Geothermal Congress 2015* 55(April):11.

Lecampion, Brice, Daniel Quesada, Matteo Loizzo, Andrew Bunger, James Kear, Laure Deremble, and Jean Desroches. 2011. "Interface Debonding as a Controlling Mechanism for Loss of Well Integrity: Importance for CO2 Injector Wells." in *Energy Procedia*.

Misaelides P, Godelistas A Link F, Bauman H. 1991. "Stepwise Dehydration of Heulandite-Clinoptilolite from Succor Creek, Oregon, USA: A Single-Crystal X-Ray Study at 100K." *American Mineralogist* 76(11–12):1872–83.

Misaelides P, Godelistas A Link F, Bauman H. 2016. "Calcining Natural Zeolites to Improve Their Effect on Cementitious Mixture Workability." *Cement and Concrete Research* 85:102–10.

Phoo-Ngernkham, Tanakorn, Sakonwan Hanjitsuwan, Nattapong Damrongwiriyanupap, and Prinya Chindaprasirt. 2017. "Effect of Sodium Hydroxide and Sodium Silicate Solutions on Strengths of Alkali Activated High Calcium Fly Ash Containing Portland Cement." *KSCE Journal of Civil Engineering* 21(6):2202–10.

Phoo-ngernkham, Tanakorn, Chattarika Phiangphimai, Darrakorn Intarabut, Sakonwan Hanjitsuwan, Nattapong Damrongwiriyanupap, Long yuan Li, and Prinya Chindaprasirt. 2020. "Low Cost and Sustainable Repair Material Made from Alkali-Activated High-Calcium Fly Ash with Calcium Carbide Residue." *Construction and Building Materials* 247.

Phoo-Ngernkham, Tanakorn, Vanchai Sata, Sakonwan Hanjitsuwan, Charoenchai Ridtirud, Shigemitsu Hatanaka, and Prinya Chindaprasirt. 2015. "High Calcium Fly Ash Geopolymer Mortar Containing Portland Cement for Use as Repair Material." *Construction and Building Materials* 98:482–88.

Pyatina, T., T. Sugama, J. Moon, and S. James. 2016. "Effect of Tartaric Acid on Hydration of a Sodium-Metasilicate-Activated Blend of Calcium Aluminate Cement and Fly Ash F." *Materials* 9(6).

Pyatina, T., T. Sugama, and T. Zaliznyak. 2017. "Durability of Bond between High-Temperature

Cement Composites and Carbon Steel." in *Transactions - Geothermal Resources Council*. Vol. 41.

Pyatina, Tatiana and Toshifumi Sugama. 2019. "Chapter Role of Tartaric Acid in Chemical , Mechanical and Self-Healing Behaviors of a Calcium- Aluminate Cement Blend with Fly Ash F under Steam and Alkali Carbonate Environments at 270 ° C." 2–41.

Pyatina, Tatiana and Toshifumi Sugama. 2020. "Cements with Supplementary Cementitious Materials for High-Temperature Geothermal Wells." *Geothermics* 86.

Pyatina, Tatiana, Toshifumi Sugama, and A. Ronne. 2016. "Self-Repairing Geothermal Well Cement Composite." *Geothermal Resource Council Transactions* 40:235–43.

Stern, M. and A. L. Geary. 1975. "Electrochemical Polarization I. A Theoretical Analysis of the Shape of Polarization Curves." *Journal of the Electrochemical Society* 104:56–62.

Sugama, Toshifumi and Tatiana Pyatina. 2017. "Bond Durability of Carbon-Microfiber-Reinforced Alkali-Activated High-Temperature Cement Adhering to Carbon Steel." *Engineering* 09(02):142–70.

Sugama, Toshifumi and Tatiana Pyatina. 2019a. "Self-Healing, Re-Adhering, and Carbon-Steel Corrosion Mitigating Properties of Fly Ash-Containing Calcium Aluminum Phosphate Cement Composite at 300 °C Hydrothermal Temperature." *Cement and Concrete Composites*.

Sugama, Toshifumi and Tatiana Pyatina. 2019b. "Self-Healing, Re-Adhering, and Corrosion-Mitigating Inorganic Cement Composites for Geothermal Wells at 270-300degC." *BNL-2019-IR*.

Teodoriu, C., C. Kosinowski, M. Amani, J. Schubert, and A. Shadravan. 2013. "Wellbore Integrity and Cement Failure at HPHT Conditions." *International Journal of Engineering and Applied Sciences* 2:1–13.

Wise, J., A. Cedola, R. Nygaard, G. Hareland, A. Oystein, Lohne HP, and EP Ford. 2020. "Wellbore Characteristics That Control Debonding Initiation and Microannuli Width in Finite Element Simulations." *Journal Od Petroleum Science and Engineering* 191:107–57.

Wolfe, M. H. 2011. "Bond Strength of High-Volume Fly Ash Concrete." Missouri S&T.

Zhijun, T., Z. Yanjun, and J. Jianghong. 2013. "Technology for Improving Life of Thermal Recovery Well Casing." *Advances in Petroleum Exploration and Development* 5:71–76.